metals

MDPI

Article

Quantitative Microstructure Prediction of Powder High-Temperature Alloy during Solution Heat Treatment and Its Validation

Zhaofeng Liu [1,2], Junyi Cheng [1,2], Chao Wang [2] and Jianzheng Guo [1,2,*]

[1] State Key Laboratory of Powder Metallurgy, Central South University, Changsha 410083, China; liuzhaofeng@csu.edu.cn (Z.L.); cjunyi@hotmail.com (J.C.)
[2] Shenzhen Wedge Central South Research Institute Co., Ltd., Shenzhen 518035, China; wangchao1234142@hotmail.com
* Correspondence: 218062@csu.edu.cn

Abstract: Heat treatment, particularly solution heat treatment, is a critical process in the preparation of powder metallurgy superalloys, where the cooling process significantly impacts the microstructure. This study, based on thermodynamic and kinetic databases as well as the precipitation mechanism of strengthening phases, delves into the influence of cooling process, especially the cooling path, on the material's microstructure. The results indicate that under slow cooling rates, the precipitated phases are more likely to exhibit a multimodal size distribution, while under rapid cooling rates, a unimodal distribution may form. The average cooling rate does not consistently accurately reflect the growth of the precipitated phases; even with the same average cooling rate, different cooling paths can lead to significant differences in the size of the precipitates. To accurately predict the size of the precipitates, it is necessary to consider the specific cooling process. Constant cooling rate experiments designed for the study and the dissection testing of full-size turbine discs produced in manufacturing validated the calculated results of the precipitates. Therefore, optimizing cooling through simulation calculations can effectively and accurately control the precipitates, thereby obtaining a microstructure that can meet performance requirements.

Keywords: solution heat treatment; cooling path; calculations; powder metallurgy superalloy

Citation: Liu, Z.; Cheng, J.; Wang, C.; Guo, J. Quantitative Microstructure Prediction of Powder High-Temperature Alloy during Solution Heat Treatment and Its Validation. *Metals* **2024**, *14*, 769. https://doi.org/10.3390/met14070769

Academic Editor: Jose Manuel Torralba

Received: 3 June 2024
Revised: 25 June 2024
Accepted: 26 June 2024
Published: 28 June 2024

1. Introduction

Nickel-based powder metallurgy superalloys exhibit exceptional high-temperature strength, creep resistance, oxidation and corrosion resistance, as well as good fatigue and fracture toughness, making them widely used in critical hot-section components of aero engines and gas turbines, such as turbine disks [1,2]. The superior properties of nickel-based superalloys are largely attributed to their unique microstructure, particularly the presence of γ' precipitates. The γ' phase is an ordered L12 structure, typically composed of elements such as nickel (Ni), aluminum (Al), or titanium (Ti) [3,4]. The plastic deformation of metallic materials is primarily achieved through the movement of dislocations on slip planes. In nickel-based superalloys, the γ' phase enhances the material through both the shearing mechanism and the Orowan bypass mechanism [5]. The former occurs when dislocations shear through the ordered γ' phase, disrupting the atomic order and generating an elastic stress field, which increases the resistance to dislocation movement and enhances the material's strength. Conversely, when the γ' phase is fine and densely distributed, dislocations bypass rather than shear, forming Orowan loops, which also increases the material's strength. The combined effect of these two mechanisms effectively impedes dislocation motion, significantly improving the high-temperature performance of the alloy. For common high-temperature alloys used in aerospace engines or gas turbines, such as Waspaloy, Nimonic 105, and Inconel 625, the primary strengthening phase is

the γ' phase [6–8]. In contrast, for Inconel 625, it also includes the γ'' and δ phases, with the γ'' phase being metastable and potentially transforming into the δ phase under certain conditions. The volume fraction, size, and distribution of the γ' phase are critical factors affecting the performance of the final products and can be regulated through appropriate heat treatment processes [9]. Therefore, accurately revealing and controlling the kinetics of the precipitate phase holds significant theoretical and practical importance for process optimization.

The kinetic simulation of precipitate phases plays a crucial role in studying and predicting the formation, growth, and evolution of these phases within alloys, as well as their influence on material properties [10]. Such simulations are vital for optimizing heat treatment processes and enhancing material performance. Several theoretical calculation methods are currently employed in this field.

Phase-field Model: This is a powerful tool for simulating the evolution of microstructures, capable of handling complex geometries and dynamic processes. In the context of precipitation kinetics, the phase-field model can describe processes such as the nucleation, growth, and morphological evolution of precipitate phases. For instance, J.Z. Zhu et al. [11] utilized the phase-field method to study the coarsening process of γ' in Ni–Al binary alloys, while Caleb O. Yenusah et al. [12] investigated the evolution of γ'' in Inconel 625 alloy during heat treatment.

Monte Carlo (MC) Simulation: This method is based on statistical mechanics and employs random sampling techniques to study the formation and evolution of precipitate phases in alloys. MC simulation is suitable for examining the effects of temperature, composition, and other factors on the dynamic behavior of precipitate phases [13,14].

However, the most prevalent method for modeling the kinetics of precipitation is the continuum-based kinetic model [10]. Unlike the phase-field model or atomic-scale simulations, these models do not involve the complexities at the micro-level of materials. Due to their abstract nature, they allow for simpler mathematical expressions and analytical calculations, making the simulation more efficient. Furthermore, their prediction results are easily compared with macroscopic experimental data, thereby facilitating the evaluation of the model's accuracy.

2. Kinetic Models of Precipitate Phases

Based on the research of Kampmann and Wagner [15], the Kampmann–Wagner Numerical (KWN) model was implemented within a numerical computational framework [16]. Expanded to handle both homogeneous and heterogeneous nucleation phenomena, as well as various morphologies of precipitates, the model aims to simulate the precipitation kinetics of multicomponent alloys under wide range of heat treatment conditions. The major components of the KWN model include nucleation, growth, and coarsening processes.

The nucleation rate is typically calculated by considering thermodynamic and kinetic parameters such as supersaturation, interfacial energy, and changes in volumetric free energy. The transient nucleation rate is usually derived from classical nucleation theory, with its core equation taking into account the free energy barrier to nucleation and the thermodynamic and kinetic properties of atoms or molecules. For homogeneous nucleation, the expression for the classical nucleation rate can generally be written as follows [17]:

$$J = N_v Z \beta^* \exp\left(-\frac{\Delta G^*}{k_B T}\right) \exp\left(-\frac{\tau}{t}\right), \tag{1}$$

where N_v is the nucleation site density, Z is the Zeldovich factor, β^* is the atomic attachment rate, τ is the incubation time for nucleation, k_B is the Boltzmann constant, T is the temperature, and t represents time. The nucleation barrier can be expressed as

$$\Delta G^* = \frac{16\pi}{3} \frac{\sigma_{\alpha\beta}^3}{(\Delta G_V + \Delta G_S)^2}, \tag{2}$$

where $\sigma_{\alpha\beta}$ is the interfacial energy between the matrix and the precipitates, ΔG_V is the volumetric chemical driving force for nucleation, and ΔG_S is the elastic strain energy per unit volume of the precipitates [18].

The growth of a precipitate, following nucleation, refers to the increase in size. The KWN model typically employs a diffusion-controlled growth, which implies that the growth of the precipitate phase is limited by the diffusion rate of solute atoms in the surrounding matrix, a rate that is significantly influenced by temperature and chemical driving force [19]. The growth of spherical or lenticular precipitates can be simplified for the curved interface as follows:

$$v = \frac{dR}{dt} = \frac{K}{R}\Delta G_m^*, \tag{3}$$

where K is the kinetic parameter, ΔG_m^* is the transformation driving force, defined as $\Delta G_m^* = \Delta G_m - \Delta G_T$, ΔG_m is the molar chemical driving force, and $\Delta G_T = \frac{2\sigma V_m}{R}$ is used to compensate for the energy difference caused by the Gibbs–Thompson effect, with σ being the interfacial energy, V_m the molar volume, and R the gas constant.

The KWN model, building upon the foundation of the modified Langer–Schwartz (MLS) model [20], further calculates the evolution of precipitate size distribution over time, thus providing more accurate predictions including key parameters such as number density, particle size distribution, volume fraction, and composition [16]. Numerous scholars have conducted related research. For instance, Radis et al. [21] studied the distribution of the γ' precipitate phase in U720Li alloy under different cooling rates through experimental methods and compared the results with those obtained from KWN precipitate kinetics calculations, validating the accuracy of the results. Liu et al. [22] reviewed the current state of simulation studies on the mechanism of precipitate formation during the heat treatment process of metallic materials, where the characteristics and future prospects of the KWN model were discussed in detail.

This study is based on the aforementioned theoretical models as well as the kinetic and thermodynamic databases, to calculate the microstructure evolution during its solution heat treatment process. It will also investigate the microstructural patterns of actual disk components under different cooling paths. The aim is to provide effective guidance for optimizing the heat treatment process of the product.

3. Microstructure Simulation and Analysis

In this study, a tailored thermodynamic and kinetic database for the nickel-based alloy system was utilized. This database, which builds upon CompuTherm LLC's nickel-based database, has been fine-tuned and optimized through the CALPHAD approach and experimental data relevant to the alloys being studied (as detailed in Table 1). It encompasses 27 elements and 343 phases, offering in-depth information on phase equilibria for each component and its potential compounds [16].

Table 1. The composition of the Ni-based alloy.

Element	Al	Co	Cr	Mo	Nb	Ti	W	Ta	Hf	Ni
Wt.%	3.0	19	13	4.0	1.2	3.7	4.0	1.0	0.2	bal.

The specific mix of elements within an alloy significantly impacts its mechanical attributes, such as strength and creep resistance. For instance, aluminum and titanium are frequently utilized to produce the γ' strengthening phase, a vital element in augmenting the high-temperature strength and creep resistance of nickel-based superalloys. Furthermore, cobalt and chromium contribute to the alloy's resistance to oxidation and corrosion, with chromium playing a crucial role in enhancing strength. The inclusion of elements like molybdenum, tungsten, and niobium further increases the alloy's creep resistance and high-temperature durability.

This extensive database lays down a thermodynamic groundwork for analyzing the precipitation kinetics of the L12_FCC (face-centered cubic) phase.

For the thermodynamic simulation of the precipitate phase, Pandat 2022a software is employed, which is based on the theoretical framework of the KWN model, with the assumption that the precipitate phase has a spherical morphology. It utilizes an improved homogeneous nucleation theory to describe the nucleation mechanism and relies on a simplified kinetic model to depict the growth process of the precipitate phase. The experimental design includes a study on the effects of different cooling paths during the solid solution cooling process on the precipitation behavior. Specifically, the research will evaluate the changes in precipitation behavior from slow cooling (5 °C/min) to rapid cooling (480 °C/min) at a fixed cooling rate; explore the impact of different cooling paths on the precipitation kinetics under the premise of equivalent average cooling rates; and investigate the effects of cooling paths on the precipitate phase in full-scale disk specimens under actual solid solution treatment conditions. Through this comprehensive study, the aim is to deeply reveal the influence of different cooling conditions on the precipitation kinetics of the γ' precipitate in the alloy system, thereby providing theoretical guidance for the optimization of the microstructure during heat treatment processing.

3.1. Microstructure under Constant Cooling Rate

The evolution of the microstructure at a constant cooling rate is of great importance for powder metallurgy superalloys. This section will investigate the behavior of precipitation by setting different constant cooling rates (5 °C/min, 20 °C/min, 60 °C/min, 200 °C/min, 480 °C/min) through precipitation kinetics simulation. The study will include the temperature range of precipitation, size distribution, and evolution process and will be validated by experiments with small samples.

3.1.1. Precipitation Temperature and Nucleation Rate

As indicated by the calculation results in Figure 1, there is a close relationship between the cooling rate and the precipitation behavior of the γ' phase [23]. The onset temperature for the precipitation of γ' for the studied alloy is slightly below the solvus temperature (1150 °C) from an earlier publication [24]. As the cooling rate increases from 5 °C/min to 480 °C/min, the nucleation rate of the γ' phase shows a significant upward trend, rising from 8.82×10^{16} $m^{-3}s^{-1}$ to 9.42×10^{21} $m^{-3}s^{-1}$. Concurrently, as the cooling rate continues to increase, the temperature at which the material achieves its maximum precipitation rate also gradually decreases, from 1143 °C to 1137 °C. For the temperature range of the primary precipitation, this range expands when the cooling rate is between 5 °C/min and 200 °C/min, but the variation in this temperature range becomes less pronounced when the cooling rate increases from 200 °C/min to 480 °C/min.

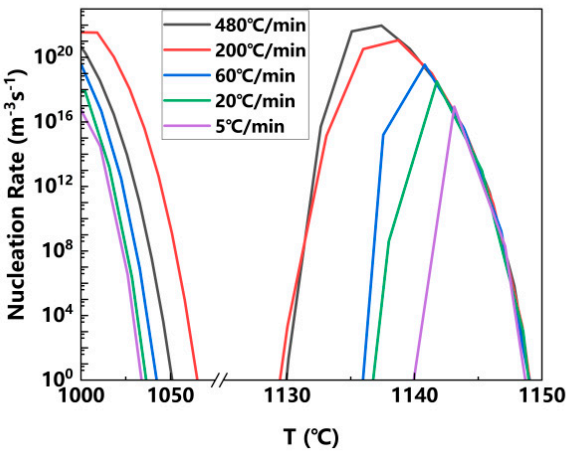

Figure 1. The precipitate nucleation rates at various cooling rates.

According to the results in Figure 2, under slow cooling conditions (such as 5 °C/min), although the low cooling rate provides a longer time for atomic diffusion [25,26], the degree of supersaturation in the material is not high, and the nucleation driving force for the precipitation phase is weak. This results in a slow formation of the γ' phase, despite it starting at a higher temperature. Conversely, rapid cooling conditions (such as 200 °C/min) significantly increase the nucleation rate. Even though rapid cooling leads to a high degree of supersaturation in the material, which restricts atomic diffusion, it also increases the driving force for the precipitation process so that once nucleation has begun, the precipitation proceeds rapidly. It is observed that at a cooling rate of 480 °C/min, the initial nucleation driving force is greater than 200 °C/min. However, as precipitation progresses, the consumption of supersaturation due to early extensive precipitation, and the possible over-suppression of atomic diffusion by the high cooling rate, lead to a nucleation driving force that gradually becomes less than that at 200 °C/min. This also explains why, during subsequent precipitation, the precipitation temperature is higher and the nucleation rate is greater at a cooling rate of 200 °C/min compared to that of 480 °C/min.

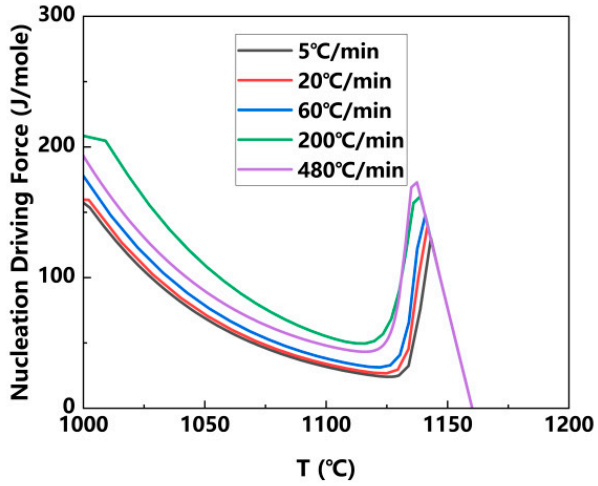

Figure 2. The nucleation driving forces under different cooling rates.

3.1.2. Multimodal Distribution of Precipitate Phases

As shown in Figure 3, cooling rates have a significant impact on the distribution characteristics of the γ' phase [27–29], especially at lower cooling rates, such as 5 °C/min, where a multimodal distribution pattern of the γ' phase is observed. During the initial high-temperature stage of cooling, due to the strong atomic diffusion, a large-sized γ' phase can quickly form and grow. As the temperature gradually decreases, smaller precipitate phases begin to appear at existing or newly formed nucleation sites. Since the temperature is lower at this time, the migration speed of atoms slows down, leading to the formation of a smaller γ' phase, thus resulting in a multimodal distribution characteristic [21,27,30–32].

In contrast, under high cooling conditions, such as a cooling rate of 480 °C/min, the diffusion process in the material is severely suppressed. The movement of atoms or molecules is restricted, leading to a rapid increase in the supersaturation of the solid solution and the formation of a large number of fine nucleation centers in the material. Due to the limitations of the diffusion process, these nucleation centers may not have enough time to grow, resulting in the formation of uniformly sized fine precipitate phases. In such cases, the precipitate phases typically exhibit a unimodal size distribution [30,33,34], meaning that the particle sizes are relatively consistent, with a narrow distribution range. Although a single-mode size distribution can provide uniform strengthening effects [35], in certain scenarios where materials need to operate at high temperatures for long periods, these fine particles may not be stable enough. Over time, these particles might coarsen, consequently affecting the stability of the material's performance.

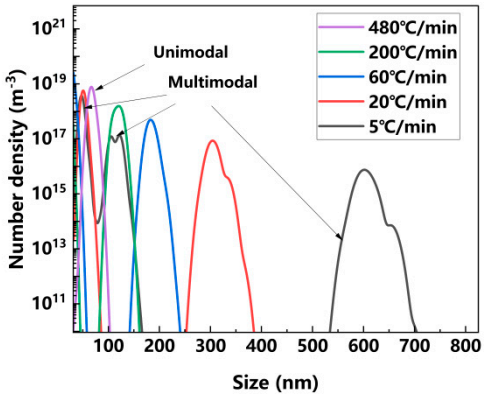

Figure 3. The particle size distributions (PSDs) at various cooling rates.

3.1.3. The Evolution Process of the γ' Phase

As shown in Figure 4 and in conjunction with Figure 1, it can be understood that during a precipitation process, for a slower cooling rate (such as 5 °C/min, Figure 4a), the nucleation rate is lower, and the size of the precipitate phase rapidly grows (from approximately 400 nm at 1130° C to 550 nm at 1070 °C). In contrast, for a faster cooling rate (such as 480 °C/min, Figure 4b), with a higher nucleation rate, the main precipitate phase consists of smaller-sized particles (with the same temperature change, from 1130 °C to 1070 °C, the size increases slightly from 40 nm to 60 nm).

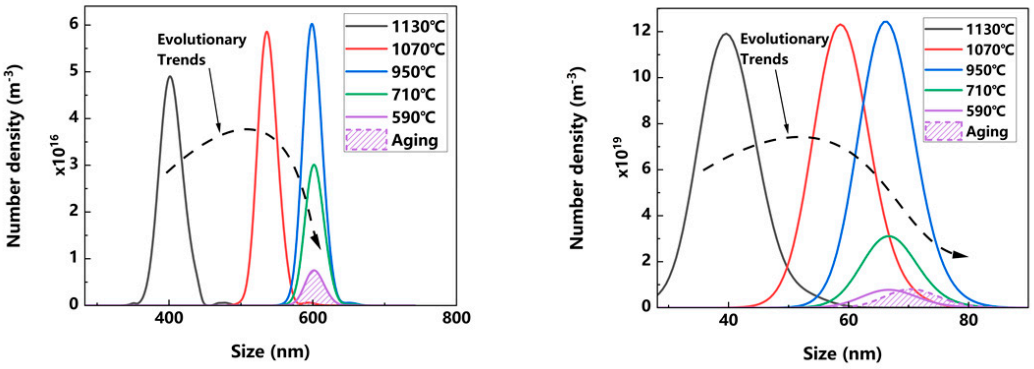

(**a**) (**b**)

Figure 4. The PSD at different temperatures under different cooling rates: (**a**) 5 °C/min; (**b**) 480 °C/min.

During the quenching process of an alloy with a constant cooling rate of 5 °C/min (or 480 °C/min), the changes in the particle size distribution of γ' at different temperatures are observed. Overall, as the temperature decreases, the formation and evolution of γ' are as follows.

For a slower cooling rate, in the high-temperature stage, atoms have higher diffusion capabilities, which promote the nucleation and rapid growth of γ'. Large-sized precipitate phases begin to form at this stage, and the increase in the volume fraction of the precipitate phase is mainly influenced by atomic diffusion. For a faster cooling rate, at the initial stage, atomic diffusion is inhibited, but a high degree of supersaturation leads to a large number of nuclei. Since the growth is minimal, the volume fraction is mainly influenced by the nucleation rate. When the temperature drops to a certain level, smaller particles may dissolve, while larger particles continue to grow, leading to an adjustment in the particle size distribution of the precipitate phase. Especially during the aging process after quenching, the process of Ostwald ripening dominates [36].

In observing the aging process at different cooling rates, it becomes clear that the influence of aging is significantly weaker for slower cooling rates compared to faster ones. For example, after 8 h of aging at a cooling rate of 480 °C/min, the average particle size gradually increases from 66.7 nm to 70.9 nm. In contrast, at a cooling rate of 5 °C/min, there is virtually no change in size. This difference is closely related to the precipitation processes of the two cases. In the former (480 °C/min), the particles are smaller with a larger specific surface area and a higher degree of supersaturation in the solid solution, making them more susceptible to growth through diffusion. The latter case (5 °C/min) exhibits the opposite characteristics.

In summary, by adjusting the cooling rate and process, it is possible to control the size and distribution of the precipitate phase, thereby optimizing the mechanical properties of the material, such as strength, hardness, and toughness. In practical applications, it is necessary to design appropriate cooling processes based on the service conditions of the material and the desired properties [37,38].

3.1.4. Constant Cooling Rate Experiments

1. Experimental Methods

The experimental materials (nominal composition shown in Table 1) were melted in a vacuum induction furnace. The main process route of the alloy is Vacuum Induction Melting (VIM) + Argon Atomization (AA) + Hot Isostatic Pressing (HIP) + Hot Extrusion (HEX) + Isothermal Forging (IF).

The detailed procedure is as follows:

- Vacuum Induction Melting (VIM):

Melt the master alloy ingot in a VIM-80II vacuum induction melting furnace with a capacity of 500 kg and a working vacuum of 10^{-3} Pa.

- Argon Atomization (AA):

Produce atomized powder using VIGA equipment with a capacity of 100 kg.

- Powder Sieving and Degassing:

Sieve the powder to a fineness of 270 mesh and subject it to vacuum degassing.

- Hot Isostatic Pressing (HIP):

Fill the treated powder into a container, seal, and process in a hot isostatic press to form a cylindrical part. The HIP parameters include ramping the temperature and pressure to 1150 °C and 150 MPa over 4 h, holding for 4 h, and then cooling with the furnace.

- Hot Extrusion (HEX):

Extrude the HIP-processed cylinder into a bar with dimensions of Φ105 × 1040 mm using a 5000-ton horizontal extruder at an extrusion temperature of 1120 °C, extrusion speed of 25 mm/s, and an extrusion ratio of 5:1.

- Isothermal Forging (IF):

Forge a Φ200 mm experimental disk blank from the above bar using a 3000-ton vertical die forging hydraulic press.

- Sample Preparation:

Finally, cylindrical samples measuring φ3 × 8 mm are sectioned from the forged experimental disk blank for testing.

A Gleeble test machine was used for the solution treatment cooling rate experiment, heating at a rate of 10 °C/min to 1190 °C, and upon reaching the temperature, cooling to room temperature at rates of 5 °C/min, 20 °C/min, 60 °C/min, 200 °C/min, and 480°C/min, observed with a Sigma300 field emission scanning electron microscope. Additionally, some samples were subjected to differential thermal analysis (DTA) on a STA 504 analyzer, uniformly heating the samples from room temperature to 1500 °C, then

cooling them to room temperature at rates of 5 °C/min, 20 °C/min, and 60 °C/min, to observe changes in the differential thermal curves.

2. Experimental Results

As depicted in Figure 5, a comprehensive elucidation of the microstructural evolution of the precipitate phase was conducted within a constant cooling rate range from 5 °C per minute to 480 °C per minute. A distinct trend was observed, where the size of the precipitate phase progressively decreased with increasing cooling rates, while its spatial uniformity improved. This observation is consistent with the findings of Zhu et al. [39], who utilized experimental data from various cooling rates to establish logarithmic equations describing the relationship between the size of the precipitate phase and the cooling rate. Similarly, Li et al. [40] employed the same approach to study the FGH4097 alloy. According to Equations (1) and (3), the Kampmann–Wagner numerical (KWN) model, which fully considers thermodynamic and kinetic factors during the nucleation and growth of the precipitate phase, provides a more physically realistic and accurate description.

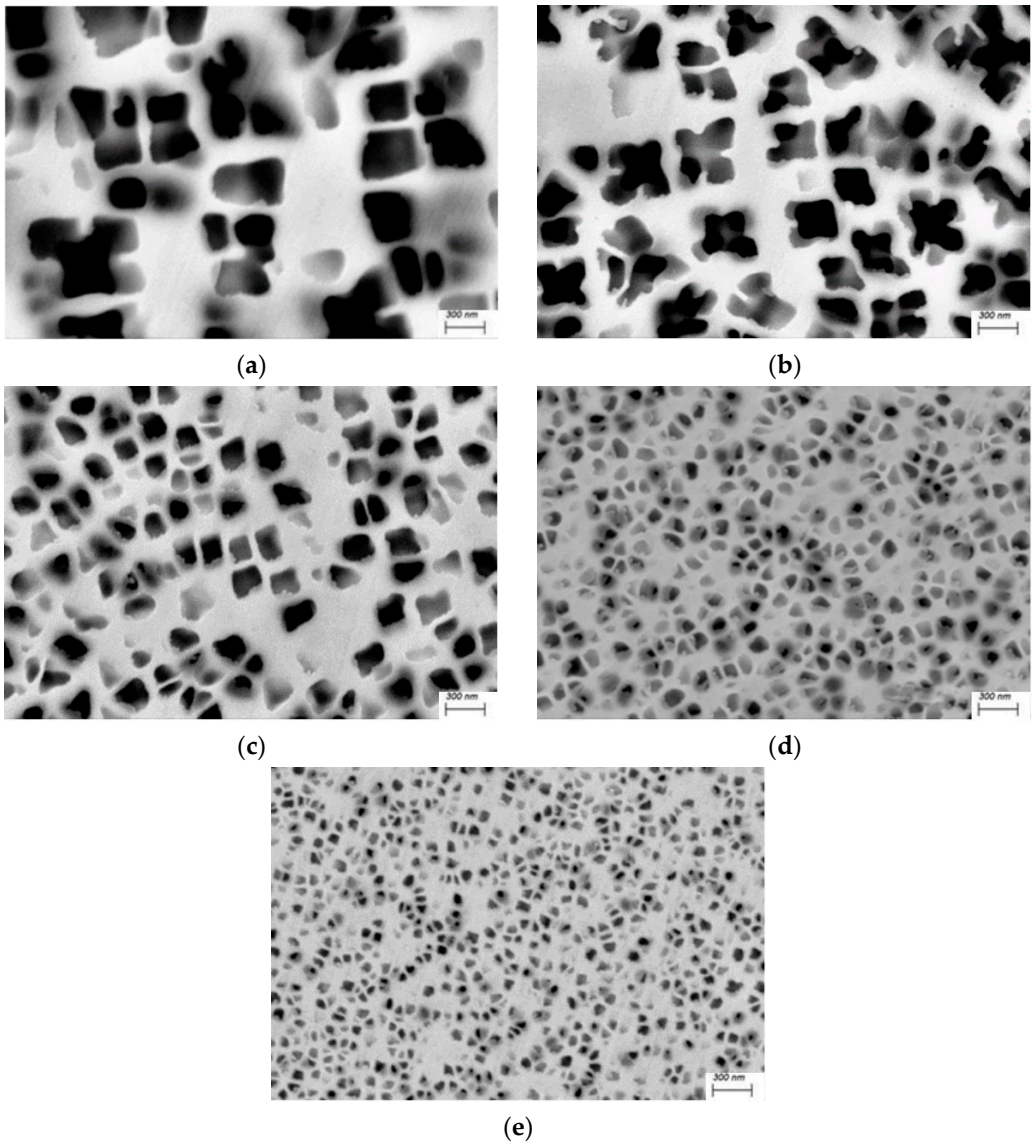

Figure 5. The distribution of the precipitated phase γ' at different cooling rates. (**a**) 5 °C/min; (**b**) 20 °C/min; (**c**) 60 °C/min; (**d**) 200 °C/min; (**e**) 480 °C/min.

The statistical analysis of the aforementioned photographs was conducted using ImageJ. The comparison between the calculated results and experimental values is shown in Figure 6. It can be seen that the calculated average sizes under different cooling rates are in good agreement with the experimental measurement.

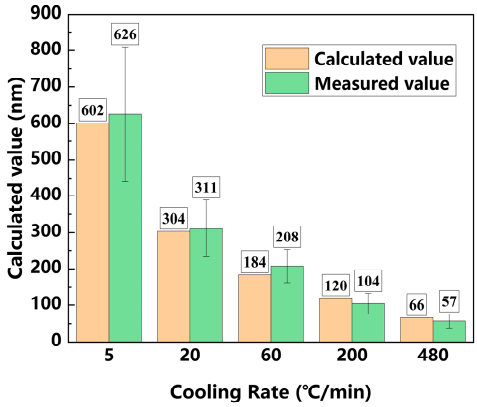

Figure 6. Comparison of experimental and calculated average sizes of γ'.

To elucidate the microstructural transformations occurring within the precipitated phases with greater clarity, Figure 7 presents Scanning Electron Microscopy (SEM) images captured in the Inlens mode following electrochemical etching, across various cooling rates. At a higher cooling rate of 200 °C/min (refer to Figure 7a), the precipitates exhibit a notably uniform and refined distribution, predominantly adopting a spherical morphology (as indicated by the blue bounding box in the figure). This phenomenon suggests that during the rapid nucleation process, the reduced duration for growth results in smaller and more uniformly dispersed precipitates.

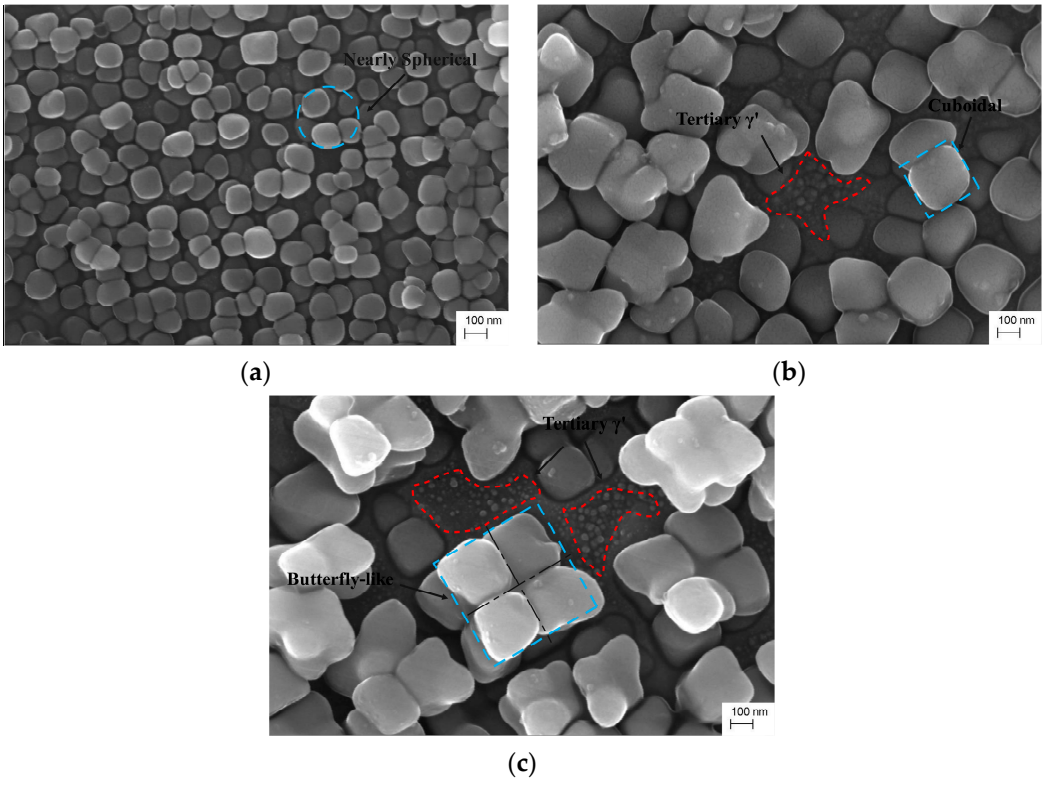

Figure 7. Electron microscope Inlens mode photographs of electrolytic etching for different cooling rates. (**a**) 200 °C/min, (**b**) 60 °C/min, (**c**) 20 °C/min.

Conversely, at a lower cooling rate, such as 20 °C/min (as shown in Figure 7c), the observed microstructural features include large-sized secondary precipitates and the formation of fine tertiary γ' precipitates within their channels, as indicated by the red dashed box in the figure. This multimodal distribution of γ' phases suggests that slower cooling rates not only promote the size growth and morphological changes of the primary phase but also permit the nucleation and growth of tertiary γ' phases in the interstices, exhibiting a spherical shape. As the cooling rate further decreases, the morphology of the secondary precipitates transitions from spherical to cuboidal (as shown by the blue box in Figure 7b) and ultimately to butterfly-shaped (as shown by the blue box in Figure 7c), reflecting the influence of cooling rate on the nucleation rate and growth kinetics of the precipitates. These observations align with the conclusions drawn by R. Radis et al. [21], who utilized the Matcalc software (https://www.matcalc.at/, accessed on 1 June 2024) to investigate the precipitation behavior of U720Li alloy under varying cooling rates. Huang et al. [41] further elucidated, through energy dispersive spectroscopy (EDS) and three-dimensional atom probe tomography (3D-APT) studies, that the decrease in cooling rate leads to the formation of elastic strain energy due to lattice mismatch, resulting in morphological changes in the secondary γ' phases. Furthermore, enrichment of different elements was observed in the channels of the multimodal γ' distribution, indicating the redistribution of elements during the γ' precipitation process, i.e., changes in solute concentration. These factors are incorporated into kinetic models to more accurately describe and predict the behavior of precipitates. These research findings collectively affirm the significant impact of cooling rate on the size and distribution of precipitates.

When a sample undergoes a phase transition (such as the dissolution or precipitation of strengthening phases), it experiences endothermic and exothermic effects, which manifest as peaks or valleys on the DTA curve. This makes DTA useful for analyzing the precipitation process of γ'. According to the differential thermal analysis (DTA) results under different cooling rates shown in Figure 8, the curve begins to decline near 1150 °C, indicating the onset of γ' phase precipitation. At a high cooling rate, such as 60 °C/min, a significant amount of γ' phase nuclei and precipitates form, resulting in distinct endothermic and exothermic peaks on the DTA curve (indicated by black arrows). This suggests that significant phase transformations occur within the material during rapid cooling, closely related to the precipitation process of the material. When the cooling rate is 5 °C/min, the DTA curve becomes flatter, indicating that at a slower cooling rate, the nucleation and precipitation processes of the γ' phase become relatively moderate, and the heat changes caused by phase transitions decrease, making the endothermic and exothermic peaks less pronounced. F. Masoumi et al. [42] used DTA to analyze the kinetic mechanism of γ' phase reprecipitation in AD730 alloy, where different cooling rates led to different precipitation peaks, with faster cooling rates resulting in larger peaks. These results are consistent with the analysis conclusion from Figure 1, indicating that the cooling rate has a significant impact on the phase transition processes within the material, which in turn affects the final microstructure and properties of the material.

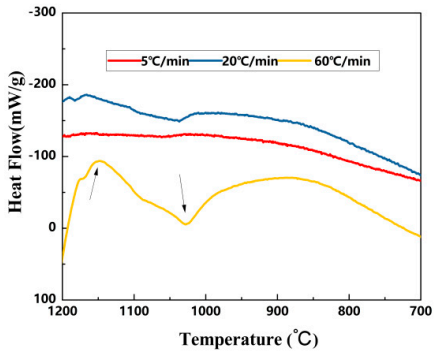

Figure 8. Differential thermal analysis curves at various cooling rates.

3.2. The Influence of Cooling Path on the Precipitation of γ'

In practical engineering applications, the concept of average cooling rate is often employed to justify heat treatment processes. The average cooling rate during quenching (Average Cooling Rate) refers to the average rate at which the material cools from the quenching temperature to a specified low temperature. For nickel-based powder high-temperature alloys, the specified low temperature is set to 800 °C normally; thus, the average cooling rate can be denoted as

$$v_{avg} = \frac{(T_s - 800) * 60}{t}, \tag{4}$$

In the formula, T_s represents the starting quenching temperature, and t denotes the time from T_s to 800 °C.

To delve deeper into the impact of the average cooling rate on the properties of nickel-based powder superalloys during the heat treatment process, we designed three sets of simulation experiments.

From Figure 9 and Table 2, it is evident that the average cooling rates of the three cooling curves between the solid solution temperature of 1160 °C and 800 °C are the same as 60 °C/min. The difference lies in the fact that for Cooling Curve 1, the average cooling rate is constantly at 80 °C/min for the first three minutes and then switches to a constant rate of 40 °C/min for the last three minutes; conversely, Cooling Curve 3 exhibits the opposite pattern; Cooling Curve 2 maintains a constant rate of 60 °C/min throughout the process.

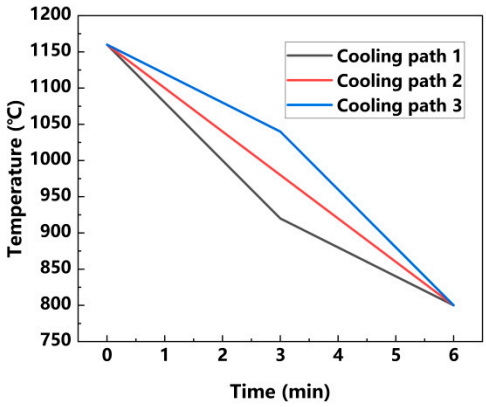

Figure 9. Three distinct cooling paths at the average cooling rate of 60 °C/min.

Table 2. The simplified cooling path at the average cooling rate of 60 °C.

Time (min)	Cooling Path 1 Temperature (°C)	Cooling Path 2 Temperature (°C)	Cooling Path 3 Temperature (°C)
0	1160	1160	1160
3	920	980	1040
6	800	800	800

As shown in Figure 10, the nucleation rates for the three cooling curves in the first nucleation interval differ: Cooling Curve 1 (1.5×10^{20} $m^{-3}s^{-1}$) has the highest nucleation rate, followed by Cooling Curve 2 (0.97×10^{20} $m^{-3}s^{-1}$), and then Cooling Curve 3 (0.32×10^{20} $m^{-3}s^{-1}$), which is consistent with the initial cooling rates.

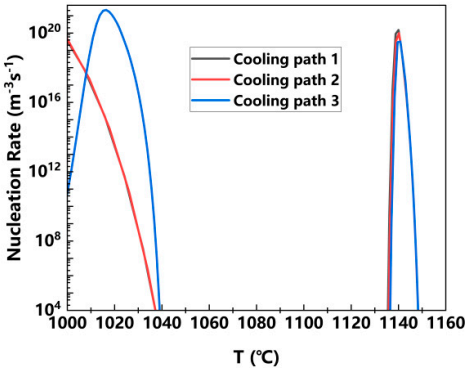

Figure 10. The nucleation rates under different cooling path conditions.

Figure 11 shows the Particle Size Distribution (PSD) at 800 °C. With a slow initial cooling rate (as in Cooling Curve 3), there are relatively fewer nucleation sites, but each nucleation site has a longer growth time, leading to the formation of larger precipitates. In contrast, rapid initial cooling (as in Cooling Curve 1) can quickly lead to a supersaturated state within the material, increasing the number of nucleation sites. However, due to the rapid cooling rate, the growth time is decreased, resulting in smaller sizes of precipitates. Cooling Curve 2, with a constant cooling rate, falls between these two extremes. The average sizes of the precipitates, following the cooling paths 3, 2, 1, are, respectively, 217 nm, 183 nm, and 166 nm.

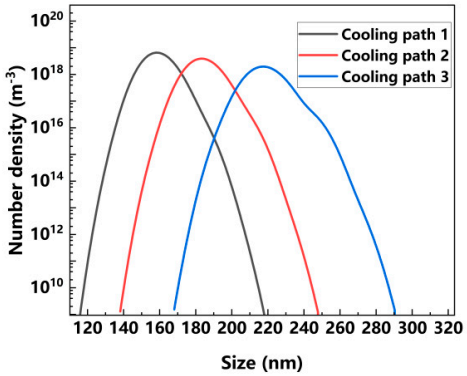

Figure 11. The PSD corresponding to different cooling paths.

In summary, although the average cooling rate provides an approximate quenching cooling rate, it does not reflect the cooling rates at different stages of the cooling process in detail, nor does it accurately describe the formation and distribution patterns of the precipitates precisely. In actual quenching processes, the cooling rate typically changes non-linearly as the temperature decreases. Such variations in cooling rates are crucial for phase transformations and the formation of precipitates in the alloy. Therefore, the size and distribution of the precipitates depend on the specific heat treatment and cooling paths experienced. The following discussion and analysis will focus on the precipitates formed under different cooling paths in the context of specific process conditions for a production disc part.

3.3. Full-Scale Disk Precipitate Evolution Simulation Analysis

In actual production processes, disc parts are usually cooled using different methods according to process requirements. Typical single cooling methods include air cooling, fan cooling, gas quenching, oil quenching, etc. [43–46]. There are also multipath cooling methods, for example, using an air furnace for oil quenching. Due to the presence of a transfer process, air cooling inevitably happens first, followed by oil quenching; as reported

in the literature [47], to reduce the risks associated with oil quenching, forced air cooling is conducted before the quenching in oil.

The following analysis is based on actual manufacturing processes to compare the solid solution cooling of full-scale disk components under different air-cooling times combined with oil quenching processes. The three-dimensional model is shown in Figure 12a; the outline dimensions are shown in Figure 12b. The air-cooling times are set at 65 s, 90 s, and 120 s. The Finite Element Method (FEM) model of the disk component is shown in Figure 12c, with three measurement points (Point1, Point2, Point3) at the middle thickness of the disk rim selected as the analysis focus areas. The horizontal positions of these points are 10 mm, 60 mm, and 120 mm from the disk rim, as shown in Figure 12b. For dual-performance powder turbine disks, the temperature field of the disk component before solid solution cooling exhibits a gradient distribution characteristic. The initial temperature distribution is determined by the preheating process; then the disk component is calculated according to different cooling paths. The initial temperature field is shown in Figure 13. The thermal boundary conditions under different paths consider natural convection heat transfer and strong radiation at high temperatures for air cooling, and intense convective heat transfer from the quenching medium for oil quenching. The cooling paths for the three measurement points under different air-cooling times combined with oil quenching are calculated using the finite element method and are shown in Figure 14.

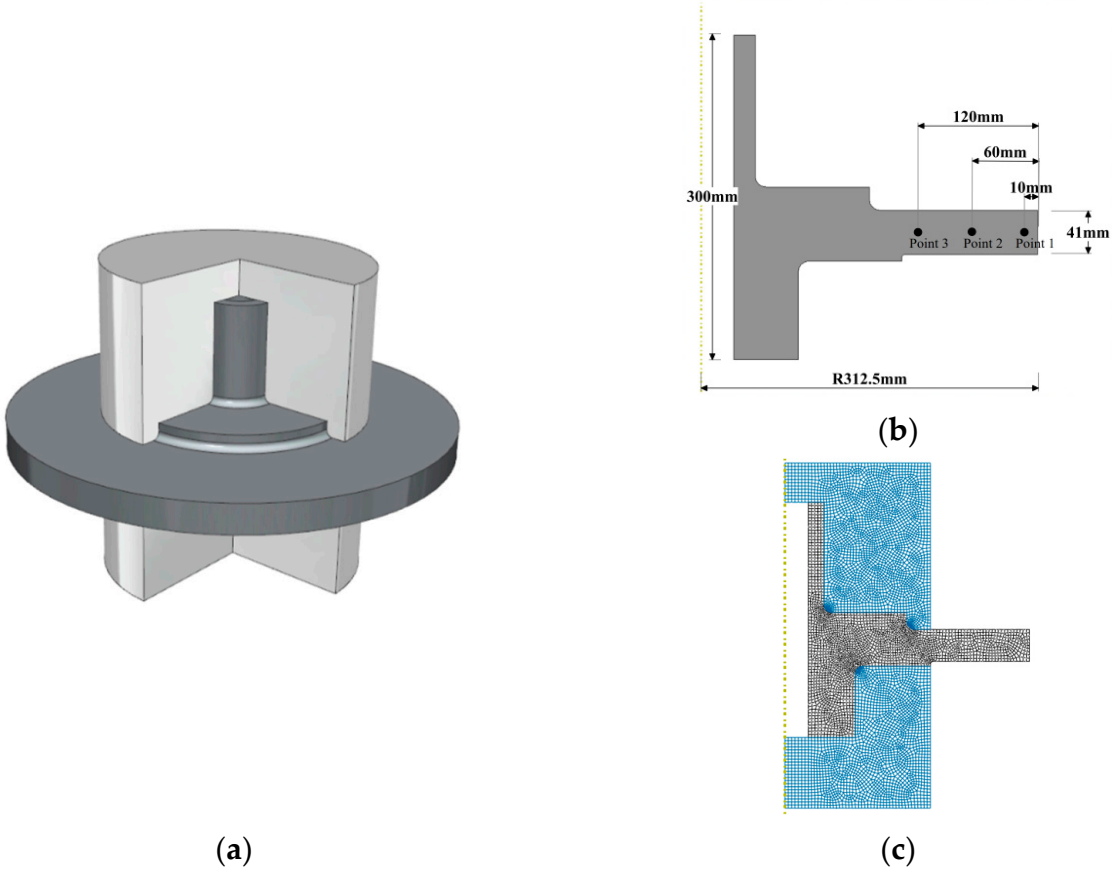

Figure 12. The computational model. (**a**) The three-dimensional model; (**b**) the outline and measurement point dimensions; (**c**) the FEM model.

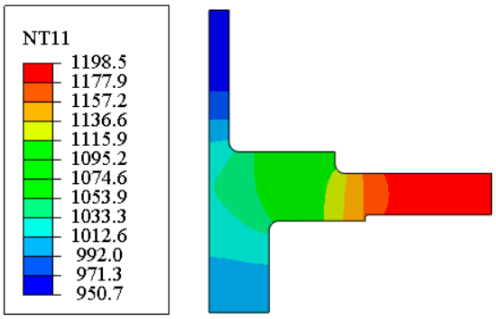

Figure 13. The temperature of the disk prior to solution quenching.

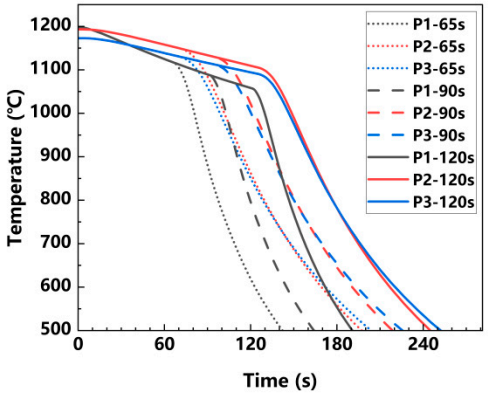

Figure 14. The three studied points' quenching paths under different air-cooling interval times.

Through kinetic calculations, the average size distribution of the precipitate phases at the measurement points under different air-cooling times is obtained and shown in Figure 15. Observations indicate that the closer to the disk rim, the smaller the average size of the precipitate phases (except for P1/P2 under 65 s air cooling + oil quenching). The shorter the air-cooling time, the smaller the average size of the precipitate phases. For the 65 s air cooling + oil quenching, the size at P2 is smaller than that of P1, as shown in Figure 16. By observing the nucleation driving force and rate at the two points during the first precipitation interval, it is found that P2 is slightly higher than P1. By extracting the cooling curves within the temperature range of the first precipitation interval (as shown in Figure 17), it can be seen that the tangent angle θ_2 at the first precipitation point is greater than θ_1, which means that the cooling rate at P2 is higher than that at P1 at this moment. Although the cooling rate of the entire curve at P1 is higher than that at P2 in the initial stage, the local cooling rate near the precipitation point affects the subsequent nucleation and growth.

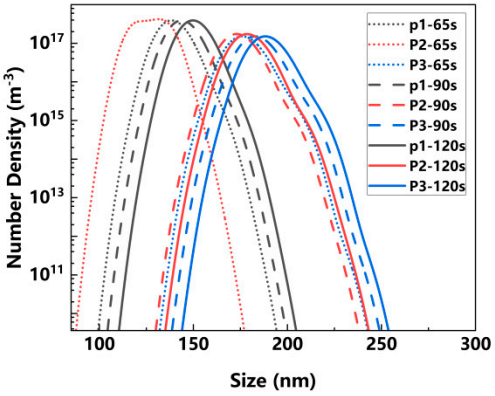

Figure 15. The particle size distribution (PSD) under different air-cooling interval times.

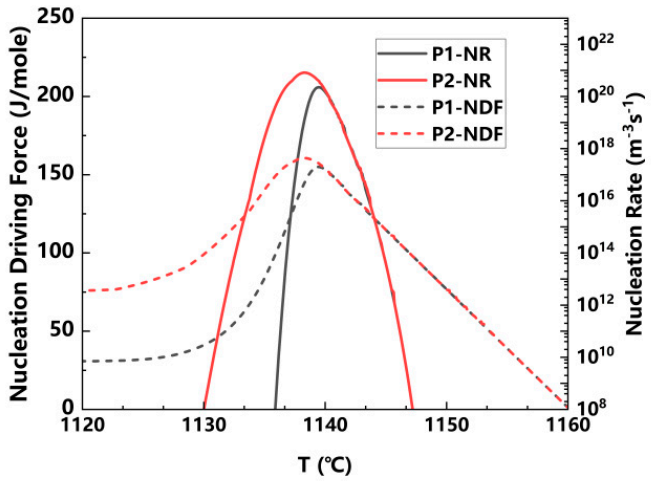

Figure 16. Nucleation driving force and rate at 65 s air-cooled P1/P2 measurement points during primary precipitation.

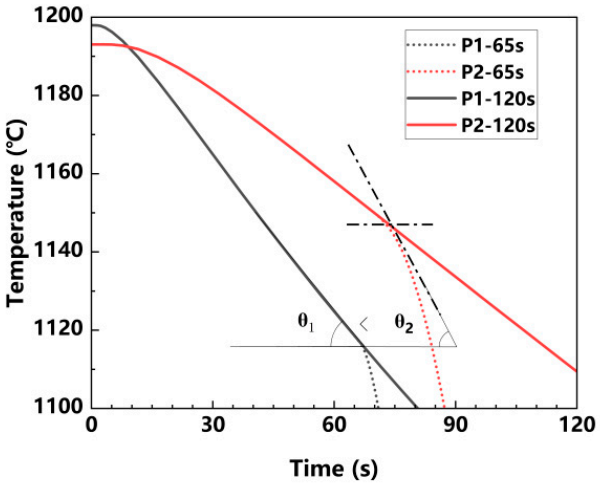

Figure 17. Temperature curves near the precipitation points P1/P2 during 65 seconds of air cooling.

In conclusion, the finite element method was employed to calculate the cooling process of disk components under various air-cooling conditions, and kinetic analysis was performed using data from three measurement points at the disk edge. Taking into account that an air-cooling duration of 120 s led to an excessively large precipitate size, and that the 65 s process was too rigorous to implement, a 90 s scheme was chosen for the validation of actual disk components.

4. Experimental Validation

The experimental disk components were drilled with thermocouple holes at predetermined measurement points along the disk edge to record the temperature changes throughout the process, as shown in Figure 18. First, the trolley furnace was heated to 1200 °C, and then the experimental disks were loaded into the furnace. Subsequently, they were heated for approximately 3 h. After the heating was completed, the disks were removed from the furnace, and the insulation fixtures were discarded. They then underwent 90 s of air cooling, followed by oil quenching. After cooling, the quenched disks were dissected for analysis. The entire experimental arrangement is shown in Table 3.

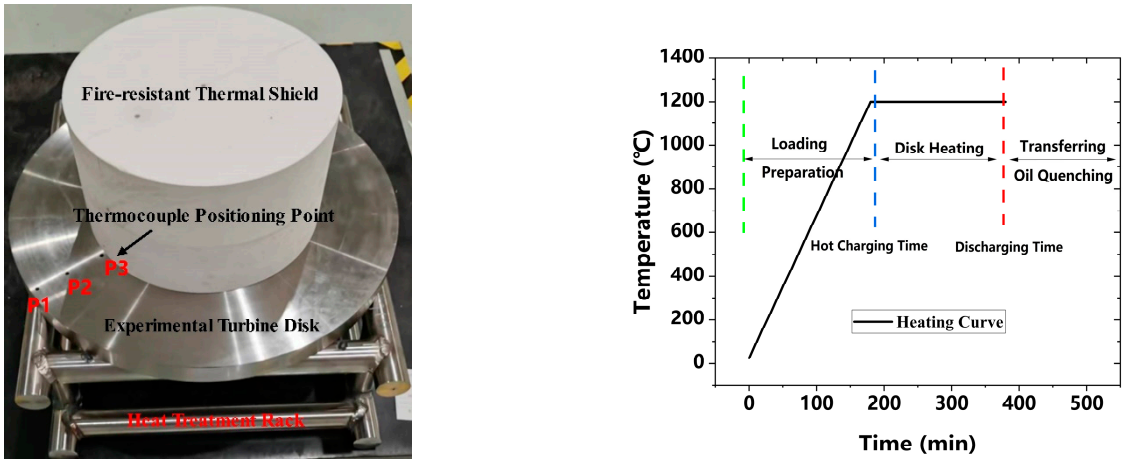

(**a**) (**b**)

Figure 18. Heat treatment experiment: (**a**) test disc; (**b**) heat treatment process.

Table 3. Experiment arrangement.

Steps:	Details:
Experimental preparation:	1. Drill temperature measurement holes, and record the temperature at the measurement points 2. Place the turbine disk, and assemble the heat-insulating tooling As show in Figure 18a
Experimental equipment:	Trolley furnace
Experimental process:	As show in Figure 18b

A comprehensive set of parameters, such as boundary conditions and the thermos-physical properties for the whole process of FEM analysis, were carefully chosen. The predicted temperature evolution from FEM analysis at the three measurement point locations are in excellent agreement with the measurements, as illustrated in Figure 19. This gives us great confidence to apply those parameters for further similar heat treatment practice. The disk components were dissected radially, and measurements were taken at the locations indicated in Figure 20. The measurement points were designated as Point1, Point2, and Point3, consistent with the positions of the points used in the calculations.

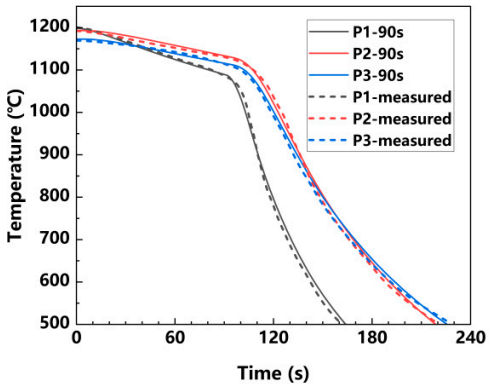

Figure 19. Comparison of experimental and simulation results for 90 s air-cooling at three measurement points.

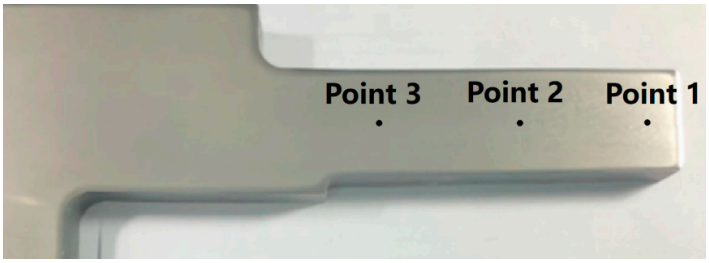

Figure 20. Measurement locations on actual anatomical specimens.

The metallographic photographs, as shown in Figure 21, were statistically analyzed using ImageJ 1.54g software, and the results were compared with the calculated ones, as shown in Table 4. The average sizes of the measured values at each measurement point are in good agreement with the calculation.

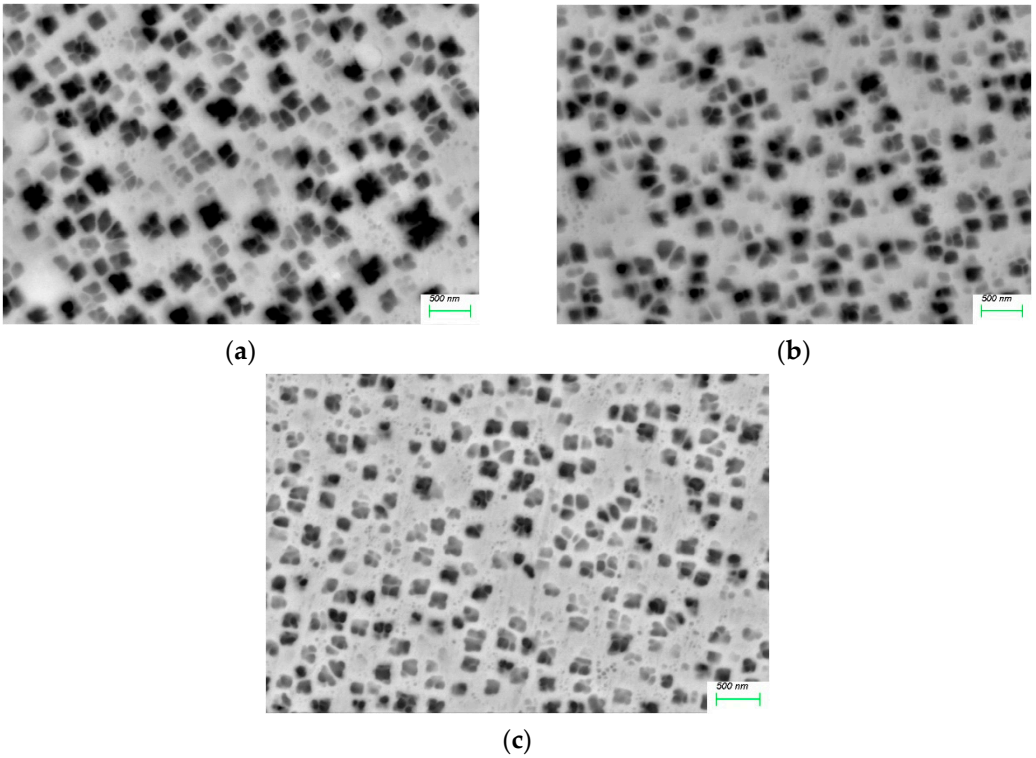

(**a**) (**b**)

(**c**)

Figure 21. Electron microscope image of γ' phase in the rim of a solution heat-treated disk at 20 Kx magnification. (**a**) Point 1 location; (**b**), Point 2 location; (**c**), Point 3 location.

Table 4. Comparison of actual disk component experiments and calculated results.

Measurement Location	Point 1	Point 2	Point 3
Measured (nm)	150	185	189
Calculated (nm)	145	173	184

5. Conclusions

Based on the analysis above, the following conclusions were reached:

1. This study conducted an in-depth quantitative analysis of the microstructural evolution mechanisms of alloys under different cooling paths by applying an advanced precipitation kinetics model. The research indicates that a high cooling rate significantly enhances the nucleation rate, thereby accelerating the formation of the γ' phase and broadening its

primary precipitation temperature range. Regarding microstructural distribution, a high cooling rate tends to result in a unimodal distribution of the γ' phase, whereas a low cooling rate facilitates the formation of a multimodal distribution. Additionally, during the early stages of the precipitation process, the kinetics of nucleation and growth of the γ' phase dominate; however, in the later stages, the coarsening mechanism becomes the primary regulator of microstructural evolution.

2. Describing the actual heat treatment process using average cooling rate has its limitations, as it cannot comprehensively reflect the complex effects of cooling paths on the size distribution of the γ' phase.
3. The high consistency between the temperature measurement of the actual disk components and the cooling paths predicted by finite element simulation provides precise boundary conditions for the numerical simulation of microstructural evolution.
4. The precise agreement between the size of the solution-precipitated γ' phase in full-size dual-property disk components for advanced aero-engines predicted by the kinetics model and the actual measurements from dissected components not only validates the accuracy of the model in predicting alloy microstructure but also provides an accurate and useful tool for optimizing the heat treatment process of disk components in engineering practice.

Author Contributions: Conceptualization: C.W.; methodology: C.W.; software: Z.L.; validation: Z.L.; formal analysis: C.W.; investigation: Z.L.; resources: J.C.; data curation: J.C.; writing—original draft preparation: Z.L.; writing—review and editing: Z.L. and J.G.; visualization: Z.L.; supervision: J.G.; project administration: J.G.; funding acquisition: J.G. All authors have read and agreed to the published version of the manuscript.

Funding: This work was supported by Shenzhen Science and Technology Major Project (KJZD20230923113900001), and the National Science and Technology Major Project (2017-IV-0009-0080).

Data Availability Statement: The original contributions presented in the study are included in the article, further inquiries can be directed to the corresponding authors.

Conflicts of Interest: All authors were employed by the company Shenzhen Wedge Central South Research Institute Co., Ltd.

References

1. Shi, C.; Zhong, Z. Forty years of Superalloy R & D in China. *Acta Metall. Sin.* **1997**, *33*, 1–8.
2. Reed, R.C. Superalloys for Turbine Disc Applications. In *The Superalloys: Fundamentals and Applications*; Cambridge University Press: Cambridge, UK, 2006; pp. 217–282. ISBN 978-0-521-07011-9.
3. Hwang, J.Y.; Banerjee, R.; Tiley, J.; Srinivasan, R.; Viswanathan, G.B.; Fraser, H.L. Nanoscale Characterization of Elemental Partitioning between Gamma and Gamma Prime Phases in René 88 DT Nickel-Base Superalloy. *Metall. Mater. Trans. A* **2009**, *40*, 24–35. [CrossRef]
4. Tiley, J.; Viswanathan, G.B.; Hwang, J.Y.; Shiveley, A.; Banerjee, R. Evaluation of Gamma Prime Volume Fractions and Lattice Misfits in a Nickel Base Superalloy Using the External Standard X-Ray Diffraction Method. *Mater. Sci. Eng. A* **2010**, *528*, 32–36. [CrossRef]
5. Wang, W.Z.; Hong, H.U.; Kim, I.S.; Choi, B.G.; Jeong, H.W.; Kim, M.Y.; Jo, C.Y. Influence of Γ′ and Grain Boundary Carbide on Tensile Fracture Behaviors of Nimonic 263. *Mater. Sci. Eng. A* **2009**, *523*, 242–245. [CrossRef]
6. Veerappan, G.; Ravichandran, M.; Marichamy, S. Mechanical Properties and Machinability of Waspaloy for Aerospace Applications—Review. *IOP Conf. Ser. Mater. Sci. Eng.* **2018**, *402*, 012039. [CrossRef]
7. Peng, T.; Wang, Y.; Yang, B.; Yang, G. Tensile Properties and Deformation Mechanisms of Nimonic 105 Superalloy at Different Temperatures. *Mater. Sci. Eng. A* **2021**, *828*, 142028. [CrossRef]
8. Shankar, V.; Bhanu Sankara Rao, K.; Mannan, S.L. Microstructure and Mechanical Properties of Inconel 625 Superalloy. *J. Nucl. Mater.* **2001**, *288*, 222–232. [CrossRef]
9. Yang, J.; Cui, J.; Cheng, J.; Xiao, L.; Guo, J. Microstructure and Mechanical Properties of a Novel Powder Metallurgy Nickel-Base Superalloy. *J. Mater. Eng. Perform.* **2023**. [CrossRef]
10. Deschamps, A.; Hutchinson, C.R. Precipitation Kinetics in Metallic Alloys: Experiments and Modeling. *Acta Mater.* **2021**, *220*, 117338. [CrossRef]

11. Zhu, J.Z.; Wang, T.; Ardell, A.J.; Zhou, S.H.; Liu, Z.K.; Chen, L.Q. Three-Dimensional Phase-Field Simulations of Coarsening Kinetics of Γ′ Particles in Binary Ni–Al Alloys. *Acta Mater.* **2004**, *52*, 2837–2845. [CrossRef]
12. Yenusah, C.O.; Ji, Y.; Liu, Y.; Stone, T.W.; Horstemeyer, M.F.; Chen, L.-Q.; Chen, L. Three-Dimensional Phase-Field Simulation of Γ″ Precipitation Kinetics in Inconel 625 during Heat Treatment. *Comput. Mater. Sci.* **2021**, *187*, 110123. [CrossRef]
13. Balbuena, J.P.; Malerba, L.; Castin, N.; Bonny, G.; Caturla, M.J. An Object Kinetic Monte Carlo Method to Model Precipitation and Segregation in Alloys under Irradiation. *J. Nucl. Mater.* **2021**, *557*, 153236. [CrossRef]
14. Kleiven, D.; Akola, J. Precipitate Formation in Aluminium Alloys: Multi-Scale Modelling Approach. *Acta Mater.* **2020**, *195*, 123–131. [CrossRef]
15. Wagner, R.; Kampmann, R.; Voorhees, P.W. Homogeneous Second-Phase Precipitation. In *Phase Transformations in Materials*; Wiley: Hoboken, NJ, USA, 2001; pp. 309–407. ISBN 978-3-527-60264-3.
16. Cao, W.; Chen, S.-L.; Zhang, F.; Wu, K.; Yang, Y.; Chang, Y.A.; Schmid-Fetzer, R.; Oates, W.A. PANDAT Software with PanEngine, PanOptimizer and PanPrecipitation for Multi-Component Phase Diagram Calculation and Materials Property Simulation. *Calphad* **2009**, *33*, 328–342. [CrossRef]
17. Russell, K.C. Nucleation in Solids: The Induction and Steady State Effects. *Adv. Colloid Interface Sci.* **1980**, *13*, 205–318. [CrossRef]
18. Clouet, E.; Nastar, M.; Sigli, C. Nucleation of Al 3 Zr and Al 3 Sc in Aluminum Alloys: From Kinetic Monte Carlo Simulations to Classical Theory. *Phys. Rev. B* **2004**, *69*, 064109. [CrossRef]
19. Morral, J.E.; Purdy, G.R. Particle Coarsening in Binary and Multicomponent Alloys. *Scr. Metall. Mater.* **1994**, *30*, 905–908. [CrossRef]
20. Semboshi, S.; Amano, S.; Fu, J.; Iwase, A.; Takasugi, T. Kinetics and Equilibrium of Age-Induced Precipitation in Cu-4 At. Pct Ti Binary Alloy. *Metall. Mater. Trans. A* **2017**, *48*, 1501–1511. [CrossRef]
21. Radis, R.; Schaffer, M.; Albu, M.; Kothleitner, G.; Pölt, P.; Kozeschnik, E. Multimodal Size Distributions of Γ′ Precipitates during Continuous Cooling of UDIMET 720 Li. *Acta Mater.* **2009**, *57*, 5739–5747. [CrossRef]
22. Feng, L.; Wang, T. Precipitation Modeling via the Synergy of Thermodynamics and Kinetics. *Acta Metall. Sin.* **2021**, *57*, 55–70. [CrossRef]
23. Babu, S.S.; Miller, M.K.; Vitek, J.M.; David, S.A. Characterization of the Microstructure Evolution in a Nickel Base Superalloy during Continuous Cooling Conditions. *Acta Mater.* **2001**, *49*, 4149–4160. [CrossRef]
24. Cheng, J.; Zhu, L.; Ma, X.; Lei, X.; Ji, H.; Guo, J. Heat treatment study on the γ″ size of a novel nickel-based superalloy. *Rare Met. Mater. Eng.* **2022**, *51*, 3722–3731. Available online: http://rmme.ijournals.cn/rmmeen/article/abstract/20210853 (accessed on 1 June 2024).
25. Papadaki, C.; Li, W.; Korsunsky, A.M. On the Dependence of Γ′ Precipitate Size in a Nickel-Based Superalloy on the Cooling Rate from Super-Solvus Temperature Heat Treatment. *Materials* **2018**, *11*, 1528. [CrossRef]
26. McLean, D. Predicting Growth of Γ′ in Nickel Alloys. *Met. Sci.* **1984**, *18*, 249–256. [CrossRef]
27. Wu, H.; Zhuang, X.; Nie, Y.; Li, Y.; Jiang, L. Effect of Heat Treatment on Mechanical Property and Microstructure of a Powder Metallurgy Nickel-Based Superalloy. *Mater. Sci. Eng. A* **2019**, *754*, 29–37. [CrossRef]
28. Klepser, C.A. Effect of Continuous Cooling Rate on the Precipitation of Gamma Prime in Nickel-Based Superalloys. *Scr. Metall. Mater.* **1995**, *33*, 589–596. [CrossRef]
29. Furrer, D.U.; Fecht, H.-J. Γ′ Formation in Superalloy U720LI. *Scr. Mater.* **1999**, *40*, 1215–1220. [CrossRef]
30. Wen, Y.H.; Simmons, J.P.; Shen, C.; Woodward, C.; Wang, Y. Phase-Field Modeling of Bimodal Particle Size Distributions during Continuous Cooling. *Acta Mater.* **2003**, *51*, 1123–1132. [CrossRef]
31. Singh, A.R.P.; Nag, S.; Hwang, J.Y.; Viswanathan, G.B.; Tiley, J.; Srinivasan, R.; Fraser, H.L.; Banerjee, R. Influence of Cooling Rate on the Development of Multiple Generations of Γ′ Precipitates in a Commercial Nickel Base Superalloy. *Mater. Charact.* **2011**, *62*, 878–886. [CrossRef]
32. Singh, A.R.P.; Nag, S.; Chattopadhyay, S.; Ren, Y.; Tiley, J.; Viswanathan, G.B.; Fraser, H.L.; Banerjee, R. Mechanisms Related to Different Generations of Γ′ Precipitation during Continuous Cooling of a Nickel Base Superalloy. *Acta Mater.* **2013**, *61*, 280–293. [CrossRef]
33. Wen, Y.H.; Wang, B.; Simmons, J.P.; Wang, Y. A Phase-Field Model for Heat Treatment Applications in Ni-Based Alloys. *Acta Mater.* **2006**, *54*, 2087–2099. [CrossRef]
34. Shahriari, D.; Sadeghi, M.H.; Akbarzadeh, A. Γ′ Precipitate Dissolution during Heat Treatment of Nimonic 115 Superalloy. *Mater. Manuf. Process.* **2009**, *24*, 559–563. [CrossRef]
35. Papon, P.; Leblond, J.; Meijer, P.H.E. *The Physics of Phase Transitions: Concepts and Applications*; Springer: Berlin/Heidelberg, Germany, 2006; p. 409.
36. Wagner, C. Theorie Der Alterung von Niederschlägen Durch Umlösen (Ostwald-Reifung). *Z. Elektrochem. Berichte Bunsenges. Phys. Chem.* **1961**, *65*, 581–591. [CrossRef]
37. Li, F.; Fu, R.; Yin, F.; Feng, D.; Wang, H.; Tian, Z.; Du, G.; Feng, Y. Impact of Solution Heat Treatment on Microstructure and Creep Behavior of a Novel Cast & Wrought FGH4096 Turbine Disk Alloy. *Mater. Sci. Eng. A* **2017**, *696*, 273–282. [CrossRef]
38. Laurence, A.; Cormier, J.; Villechaise, P.; Billot, T.; Franchet, J.-M.; Pettinari-Sturmel, F.; Hantcherli, M.; Mompiou, F.; Wessman, A. Impact of the Solution Cooling Rate and of Thermal Aging on the Creep Properties of the New Cast & Wrought René 65 Ni-Based Superalloy. In Proceedings of the 8th International Symposium on Superalloy 718 and Derivatives, Pittsburgh, PA, USA, 28 September–1 October 2014; pp. 333–348.

39. Zhu, L.; Pan, H.; Cheng, J.; Xiao, L.; Guo, J.; Ji, H. Dendrite Evolution and Quantitative Characterization of Γ′ Precipitates in a Powder Metallurgy Ni-Based Superalloy by Different Cooling Rates. *J. Alloys Compd.* **2022**, *918*, 165677. [CrossRef]
40. Li, P.; Chen, L.; Bu, H.; Zeng, Y.; Li, S.; Wang, C. Effect of Cooling Rate on the Morphological Changes in the Secondary γ′ Precipitation in FGH97 Nickel-Based PM Superalloy. *Intermetallics* **2024**, *171*, 108344. [CrossRef]
41. Huang, H.; Zhang, H.; Hu, B.; Wang, H.; Liu, G. Study on Γ′ Precipitation Behavior in a Nickel-Based PM Superalloy during Interrupted Continuous Cooling. *Intermetallics* **2020**, *116*, 106659. [CrossRef]
42. Masoumi, F.; Shahriari, D.; Jahazi, M.; Cormier, J.; Devaux, A. Kinetics and Mechanisms of Γ′ Reprecipitation in a Ni-Based Superalloy. *Sci. Rep.* **2016**, *6*, 28650. [CrossRef]
43. Gayda, J.P.; Lemsky, J. Assessment of NASA Dual Microstructure Heat Treatment Method for Multiple Forging Batch Heat Treatment. 2004. Available online: https://ntrs.nasa.gov/citations/20040040179 (accessed on 1 June 2024).
44. Mourer, D.P.; Williams, J.L. Dual Heat Treat Process Development for Advanced Disk Applications. In Proceedings of the International Symposium on Superalloys, Champion, PA, USA, 19–23 September 2004; pp. 401–407. [CrossRef]
45. Ganesh, S.; Tolbert, R.G. Differentially Heat Treated Article, and Apparatus and Process for the Manufacture Thereof. US Patent 5,527,020, 18 June 1996.
46. Gayda, J.; Gabb, T.P.; Kantzos, P.T. Heat Treatment Devices and Method of Operation Thereof to Produce Dual Microstructure Superalloy Disks. 2003. Available online: https://ntrs.nasa.gov/citations/20040015213 (accessed on 1 June 2024).
47. Gayda, J.; Gabb, T.; Kantzos, P.; Furrer, D. Low Cost Heat Treatment Process for Production of Dual Microstructure Superalloy Disks. 2003. Available online: https://ntrs.nasa.gov/api/citations/20030022720/downloads/20030022720.pdf (accessed on 1 June 2024).